Real-time Process Operation Evaluation and Model Reliability Assessment for Chemi-thermomechanical Pulping Process

Mengqi Fang[a], Ejaz Wattoo[b], Brendon Palmer[b], Darren Guliov[b], Paul Bicho[b], Yankai Cao[a], Vijay Kumar Pediredla[a] *, Bhushan Gopaluni[a] *

[a] Department of Chemical and Biological Engineering, The University of British Columbia, Vancouver, Canada

[b] Canfor Pulp, Burnaby, Canada

Abstract

In this paper, a real-time chemi-thermomechanical pulping (CTMP) process was investigated, where opportunities were explored to increase energy consumption efficiency with a guarantee of expected pulp properties as a priority. Due to the process instrumentation limitations, such as the lack of advanced regulatory controllers and optimization units, the advanced process controllers and real-time optimization strategies can hardly be implemented in the existing CTMP processes. Therefore, a novel visualization-based process evaluation methodology is proposed to aid the mill operators in making further decisions to improve the process operations. Additionally, to determine the desirable pulp properties for production, an inferential sensor model is developed that estimates the handsheet properties from pulp properties. Also, to assess the model prediction accuracy in real-time, a reliability index model is designed. The proposed methodologies have been validated on a practical CTMP process, and the results show the satisfactory performance of the system.

Keywords: Chemi-thermomechanical pulping process, energy consumption optimization, visualization, process operation performance evaluation, model reliability analysis

*Corresponding author: vijay.pediredla@ubc.ca

1 Introduction

The prosperity of the pulp and paper industry has been lasting for decades. In recent years, despite the proposals on paperless alternatives, the global pulp and paper market has been steadily growing at over 1% per year[1]. Among the existing pulping processes, the mechanical pulping processes are widely used for newsprint productions, owing to their relatively high pulp yield[2]. However, the mechanical pulping processes are also highly energy intensive, mainly because of the core refining segments. Also, due to the increase in electricity price, the environmental concerns, the carbon taxes, and the low energy efficiency, the research focusing on energy consumption optimization while maintaining the expected pulp quality have significant attention and has been actively pursued by many research groups worldwide. In the existing literature, two typical representatives of mechanical pulping processes are commonly considered, namely, the thermo-mechanical pulping (TMP) process and the chemi-thermomechanical pulping (CTMP) process.

Various methodologies have been developed to address the energy reduction objective, where the multivariate advanced process control strategies and real-time optimization (RTO) approaches were most prevalent among the existing methodologies. Typical examples of advanced process control are the different kinds of model predictive control (MPC) strategies developed to regulate the TMP processes. Tian et al. specifically proposed multi-objective economic MPC strategies with state estimation to address the trade-off between the economic and set-point tracking performance[3, 4, 5]. In the series of works proposed by Harinath et al.[6, 7, 8], economic nonlinear MPC approaches are configured to deal with the real-time control and optimization in both high and low consistency refining operations of a TMP process. Other MPC approaches have also been proposed to control pulping processes, such as the simplified linear MPC strategy[9], the generalized predictive controller[10] and a recent work of inferential MPC design[11]. Moreover, to address model uncertainty and process disturbance in the kraft pulping process, well-designed offset-free MPC strategies[1, 2] have been employed to regulate the Kappa number and cell wall thickness with compensation of plant-model mismatch and system disturbances. A global linear representation based on Koopman operator theory has been implemented to describe the nonlinear dynamic kraft pulping process[3]. Qian Xingsheng[2] and Karlstrom et al.[12] first-principles models are generally used, where the former model is developed considering the operating variables, disturbances, and pulp properties, and the

latter model is entropy-based which is a division of motor load of steam production and wood chips defibration. However, these models are based on several assumptions, and there is also a risk of fiber cutting and eventually a plate clash[13]. In parallel with the MPC-related approaches, many RTO approaches also exist to guide pulp mill operations. For instance, Mercangöz et al.[14] designed and implemented a linear programming-based economic RTO strategy, resulting in relatively high annual savings. A multivariate analysis-based TMP optimization proposed by Elsinga et al.[15] optimizes the quality parameters. In Nuengwang et al.'s work[16], the RTO approach has been implemented in three scenarios to determine optimal pulp mill operation conditions to resist the impacts of wood moisture content variations. Choi et al. proposed the multiscale modelling of fibre morphology describing the change of fiber length and cell wall thickness during pulping that captures the dynamic evolution in the paper mill process[17]. Also, some advanced interpretable machine-learning algorithms have been implemented for modelling and decision-making of pulp mill process operations[18, 19]. These proposed approaches have been validated on either simulated or practical pulping processes and gained satisfactory performances. However, restricted to the instrumentation of certain pulping processes, the existing well-designed approaches might lose their effectiveness.

In practical applications, MPC and RTO strategies require appropriate infrastructure support from pulp mills, including software and hardware configurations. The calculated optimal steady-state operating conditions are achievable when multivariate controllers are accessible to stabilize the process. The dynamic optimization in MPC can set the manipulated variable operations, but it must have the support of an online optimizer and executors to realize the received commands with specified sampling rates. However, for the CTMP process investigated in this paper, only basic closed-loop controllers are set up in the mill with critical set points provided by the process operators. The lack of multivariate advanced control configuration restricts the economic MPC implementation. Also, the static RTO can hardly perform well due to the missing stabilizing controllers. Instead of using an online optimizer to provide an optimal solution, we develop a non-interactive approach to evaluate the process operation performance in real-time using visualization methodology. Motivated by the existing optimization approaches, the feasible regions of the selected manipulated variables are explored and visualized through the produced pulp quality. Using the proposed methodology, the process operators and engineers intuitively comprehend the process operations and can manipulate the process operations better according to the provided recommen-

dations, especially when the performance is degraded. The advantages of the proposed strategy include: (1) The modelling and computations are simple and straightforward to implement in an industrial operation environment; (2) Satisfactory accuracy is achievable in a simple framework and can easily be operated and maintained by mill operators; (3) Non-intrusive characteristic makes the online realization safe and effective; (4) Intuitive visualization integrated with high-dimensional information is easily understood and accepted by mill operators; (5) The proposed framework has high extensibility and easily be upgraded to incorporate more advanced techniques. Finally, to the best of the author's knowledge, the proposed methodology is the first among the works on visualization-based mechanical pulping process operation performance evaluation.

Owing to the effective online pulp analyzers, the pulp property relevant measurements, such as pulp freeness and shives, are accessible with a regular sampling rate; therefore, it makes the real-time pulp quality closed-loop control feasible. However, controlling the pulp properties is still an intermediate target, based on which the lab-measured handsheet properties, such as tensile and bulk, need to be regulated eventually. In this work, we further modelled the handsheet properties as functions of pulp properties, similar to online inferential sensors. And the prediction performance of such an inferential sensor model is evaluated online. Only a few works exist on the reliability analysis of inferential sensor models. For example, in Kaneko et al.'s work[20], the Euclidean distance of a new observation to the center of the model training data set is employed as a metric to assess the model prediction accuracy. To evaluate the prediction accuracy of partial least squares (PLS) models, Nomikos et al.[21] designed approximate confidence intervals to indicate the model reliability. Kamohara et al.[22] reformulated this problem into a multivariate statistical process monitoring framework and came up with a Hotelling T^2 statistic to diagnose the model performance degradation. In order to fully explore the model training and validation performances, the bootstrap method has been employed to generate pseudo samples and re-estimate the model several times[23]. However, these above algorithms still have their own flaws[24], and to address these issues, Khatibisepehr et al.[24] proposed a Bayesian approach to characterize the relationship between the model input space and prediction accuracy. Motivated by this existing work and considering the actual CTMP process operations in our work, a new inferential sensor model reliability methodology is developed. Compared with the existing work[24], the Bayesian model, which is used to classify the reliability levels, has been further simplified to adapt to the frequent model update and compu-

tation resource limitations. More importantly, the uncertainty of the Bayesian classifier has been quantified, and a compound metric is created as an evaluator of inferential sensor model reliability. Based on this metric, the mill operators can be guided to set desired pulp properties.

The contents of this paper are organized as follows. In section 2, the CTMP process is first introduced, followed by the detailed procedures of CTMP process modelling. Section 3 includes comprehensive explanations of the proposed visualization-based process operation evaluation approach and critical evaluation statistics. In addition to the process operation evaluation, the inferential sensor model reliability analysis is formulated in section 4. All the proposed methodologies are tested, and the performances are validated on a practical CTMP process, which is illustrated in section 5. Finally, section 6 provides the conclusions and summarizes the proposed work.

2 Chemi-thermomechanical pulping process

In this work, a continuous CTMP process is considered with a basic schematic shown in Fig. 1. A typical CTMP process is decomposed by four sequential operation components, including (1) wood chip pre-treatment; (2) two-stage high consistency refining process; (3) pulp processing and (4) pulp bleaching operations[2]. In order to convert the raw wood chips to the high-yield pulp which is qualified for paper making, the CTMP process employs both chemical addition and elevated temperature as refining operating conditions during continuous pulping. Given this scenario, understanding the impacts of the operating conditions on the final pulp qualities becomes necessary. In the following subsections, the functions of CTMP operation components, the process variable characteristics and the objectives of this work are presented in detail.

2.1 Description of CTMP process components

In general, a CTMP process usually starts from the wood chip pre-treatment component, in which a series of operations are conducted to prepare the wood chips to a refiner acceptable level. Specifically, the feed-in wood chips first passes through the screen unit to remove the fragments with unqualified sizes and then are washed to get rid of the contaminants, after which a steaming operation is conducted with pre-designed pressure, and temperature[25]. A major difference between CTMP and TMP processes happens during the wood chip pre-treatment operation, wherein the

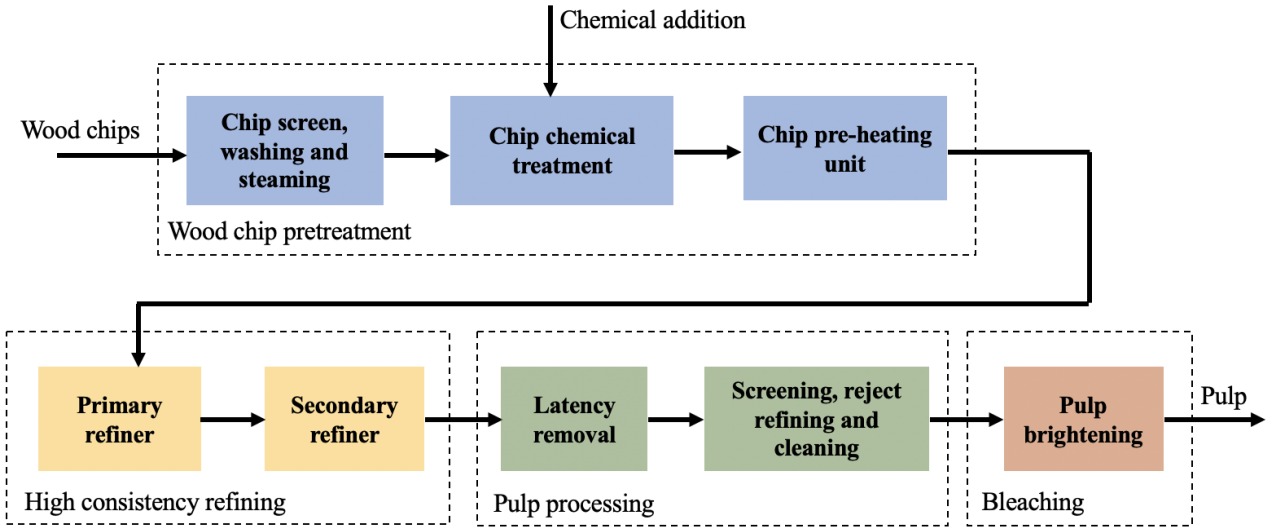

Figure 1: The schematic of a typical CTMP process

CTMP process, chemicals are added into the tank containing the processed wood chips, known as chip impregnation. This additional chemical treatment aims to enhance the pulp brightness and strength, and reduces the shive content. Thus, decreasing the energy required in the subsequent refining operations[2]. Particular wood chip pre-treatment operations, such as the steaming and pre-heating units, need predetermined pressure and temperature settings to keep the chip moisture and long fibre contents within the expected operating range[26]. However, these operating conditions vary from mill to mill and are even time-varying in a particular mill due to the feed-in wood chip quality variation. The entire pre-treatment component runs slowly to process the raw wood chips completely. In the CTMP process of this work, it usually takes 1.5 hours from the initial chip storage bin to the blowline of the primary and secondary refiners.

The two-stage refining operation closely follows the wood chip pre-treatment units and acts as a critical component in the CTMP process. Conveyed by a chip transfer screw, the pre-processed wood chips are fed into primary and secondary refiners to complete the conversions from wood chips to wood fibres and eventually to pulps. In the refining process, the rotating plates of the refiners always maintain a high intensive working load to create the refining zones, where the primary refiner can efficiently break the wood chips into fibres, and the secondary refiner can develop pulp qualities. Therefore, the two-stage refiners are the most energy intensive units throughout the CTMP process.

Meanwhile, dilution water is continuously fed into the two-stage refiners to keep a high-consistency environment in the refining zones. However, high consistencies and high temperatures throughout the refining process can make the wood fibres extremely deformed and entangled, resulting in stiff lignin and deformed fibres. As a result, latency removal is required as the key unit to deflocculate and straighten the fibres[27]. The high consistency refining and latency removal process usually cost another 1.5 hours in the investigated CTMP process.

In addition to latency removal, the pulp processing operations include screening, low-consistency refining, and cleaning procedures. After these operations, the pulps are further cleaned to a level of reduced contaminants and shives and contain more flexible long fibres. To this end, the pulp at the current stage is qualified for further bleaching and paper making. In the entire CTMP process, this paper mainly focuses on the operations from chemical impregnation to latency removal to evaluate the impacts of the process operating conditions on pulp qualities.

2.2 Main process variables

In order to provide a reliable and comprehensive evaluation of process operating conditions, the key process variables and their correlations need to be comprehended. The following contents elaborate an overview of different process variables before proceeding to the CTMP process modelling. As listed in Table 1, the available CTMP process variables include manipulated and operating variables, pulp properties and handsheet properties, and are categorized according to their functionalities and sampling frequency. Fig. 2 illustrates the sample locations and the relationships among these process variables, with shaded nodes representing the operating variables.

2.2.1 Manipulated variables and operating variables

Manipulated variables (MVs) and operating variables (OVs) play an important role in CTMP process control and optimization by deciding the process operating point and monitoring the process operation performance. Following the definitions given in the existing literature[26, 3], the MVs denote the adjustable input variables to control the CTMP refining process in real time, and the OVs represent the variables that indicate the operating conditions. The OVs depend on the MVs and can strongly impact the pulp properties. Except for the refining consistency, both MVs and OVs are accessible with a high sampling rate in this work, for example, in minute scale. The dependencies

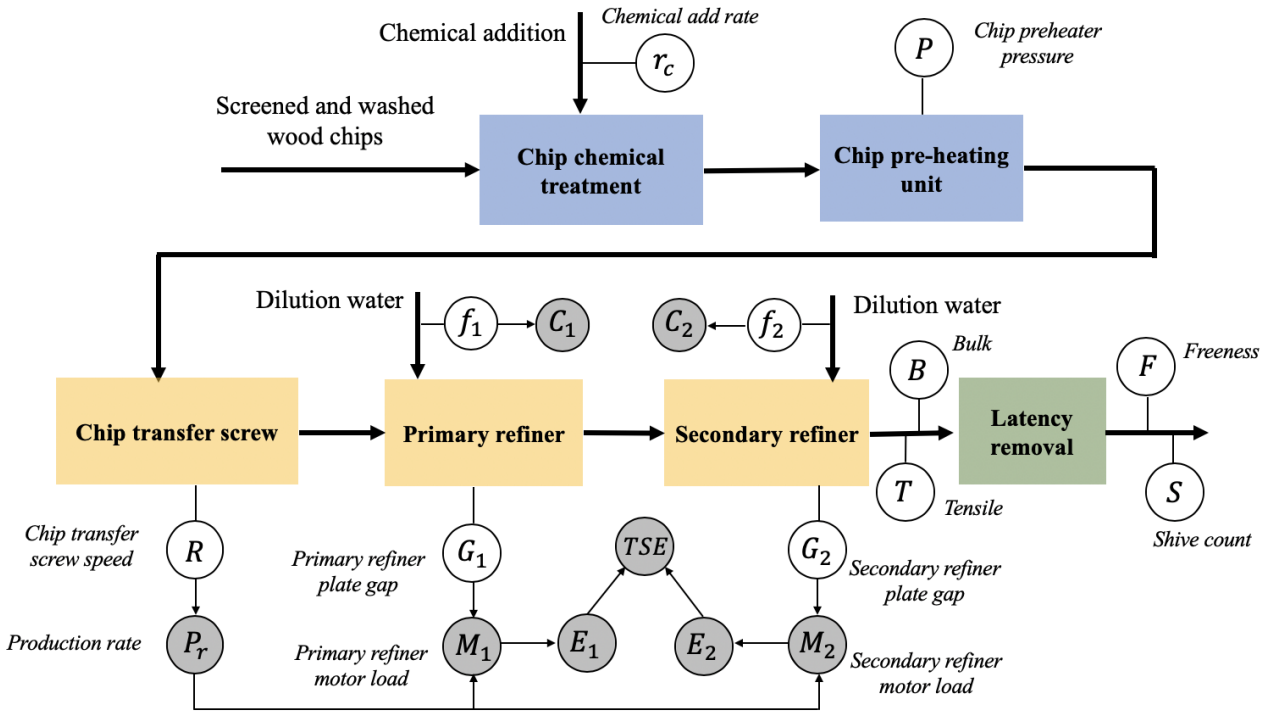

Figure 2: The illustration of the process variables in CTMP process, with shaded nodes representing the operating variables

among MVs and OVs are denoted in Fig. 2 using arrows.

(1) Chip transfer screw speed R and production rate P_r

This MV-OV pair contains one of the most important mill operating factors, namely, the production rate, which is defined as oven-dry wood flow fed into the primary refiner. It indicates the throughput of the CTMP process and also decides the pulp yield amount. The correlation between the production rate and chip transfer screw speed can be found as follows[8]:

$$P_r = 1.44 k_p s_c d_c R \tag{1}$$

where the production rate P_r $(tonnes/day)$ is proportional to the multiplications of the proportional constant k_p (m^3/rev), chip solid content s_c (%), chip bulk density d_c (kg/m^3) and chip transfer screw speed R (rpm).

However, in most cases, the wood chip quality relevant variables s_c and d_c can hardly be measured precisely. Therefore, the production rate is simply calculated by multiplying a

constant factor to the chip transfer screw speed, which also becomes the control strategy in most pulp mills to achieve the desired production rate. On the other hand, the variations of s_c, d_c and wood species turn into the dominant disturbance sources.

(2) Refiner plate gaps $G_{1:2}$, refiner motor loads $M_{1:2}$, refiner specific energies $E_{1:2}$, and total specific energy TSE

To obtain the desired pulp quality, the refiner operating conditions must be carefully adjusted with different production rates. The variables with dominant impacts on the refining processes are the refiner plate gaps, refiner motor loads and refiner specific energies, and they are also strongly correlated with each other. The plate gaps of primary and secondary refiners are defined as the separation distances between the refiner plates, which have a direct impact on the refining zone surface area. Hydraulic or electro-mechanical systems can directly control the plate gaps to achieve desired motor load and specific energy. The closer the plate gaps are, the higher the power is consumed because of higher motor loads. The following correlation between the motor load and specific energy is as follows:

$$E_i = c_e \cdot \frac{M_i}{P_r}, \qquad i = 1, 2 \tag{2}$$

where c_e is a constant for unit conversion from $MW \cdot day/tonnes$ to $kWh/tonnes$.

From the above calculation, the specific energy can be interpreted as the energy consumed when producing unit tonnes of dry pulp, which acts as a critical energy consumption indicator and also strongly affects the produced pulp quality. Higher specific energy can be achieved by increasing the motor load and keeping the production rate constant. For this two-stage refining process, the total specific energy TSE is computed by adding E_1 and E_2 and is evaluated to measure the total energy consumption of primary and secondary refiners. In many pulp refining energy optimization works, the total specific energy is the only index selected to measure economic performance.

(3) Dilution flow rates $f_{1:2}$ and refining consistencies $C_{1:2}$

Consistency in the refining zone is another important operating factor, which affects the energy-quality relationships. Refining performances at different consistencies are quite differ-

ent inspite of given specific energy. Therefore, maintaining consistency within a designated operating range is very important to improve energy conversion efficiency. Among multiple influential factors, the manipulation of dilution flow rates added to the refiners is the most convenient. The refining consistency is defined as the ratio of *dry fibre flow rate* to *fibre and water flow rate*; therefore, it cannot be directly measured online but is often inferred using a mass balance mechanism[28].

(4) Chemical add rate r_c and chip preheater pressure P

Chemical add rate and preheater pressure are another two MVs in the wood chip pre-treatment component and are rarely discussed in CTMP control strategy configuration. The change of chemical add rate r_c $(kg/tonne)$ affects the freeness and shive content of the produced pulps with given specific energy, and this index has to be optimized when performing CTMP process optimization. The preheater pressure is measured at the chip pre-heating unit, which is in upstream of the chip transfer screw, and proper adjustment of this pressure can also facilitate the downstream pulp refining operations.

Table 1: Main process variables in the CTMP refining process

Manipulated variables		Operating variables	
Description	Notation (Unit)	Description	Notation (Unit)
Chip transfer screw speed	R (rpm)	Production rate	P_r $(tonnes/day)$
Primary refiner plate gap	G_1 (mm)	Primary refiner motor load	M_1 (MW)
Secondary refiner plate gap	G_2 (mm)	Secondary refiner motor load	M_2 (MW)
Primary dilution flow rate	f_1 (kg/s)	Primary specific energy	E_1 $(kWh/tonne)$
Secondary dilution flow rate	f_2 (kg/s)	Secondary specific energy	E_2 $(kWh/tonne)$
Chemical add rate	r_c $(kg/tonne)$	Total specific energy	TSE $(kWh/tonne)$
Chip preheater pressure	P (kPa)	Primary refining consistency	C_1 (%)
		Secondary refining consistency	C_2 (%)
Pulp properties		**Handsheet properties**	
Description	Notation (Unit)	Description	Notation (Unit)
Canadian standard freeness	F (ml)	Tensile	T $(N \cdot m/g)$
Shive count	S	Bulk	B (cm^3/g)

2.2.2 Pulp properties

Several important and relevant pulp quality variables exist in the pulping process, such as Canadian standard freeness, shive content, long fibre content, strength, etc., which can affect the

final paper qualities. The desired pulp properties are defined according to the end product quality requirement, and controlled in real-time by adjusting the MVs and OVs. The pulp properties are measured by pulp online analyzers such as the PulpEye analysis system. The analyzer can provide frequent sample measurement, with a sampling rate in the hour scale. The pulp freeness is measured by collecting the water from a pulp suspension through pulp drainage, and it also represents the degree of refining done on the pulp[26]. Shive count denotes the quantity of the shives in unit gram of the pulp, which depends on the shive content, the pulp sample size, etc. It can act as an indicator of pulp strength and drainage properties. Long fibre content is another indicator that is relevant to pulp strength. Based on the practical requirements of CTMP mill operation, this work mainly focuses on the first two most important pulp properties, namely, the freeness and shive count.

2.2.3 Handsheet properties

Handsheet properties, for example, tensile, bulk, tear and burst indices, are closely related to the final paper product qualities. These variables of the handsheet quality are accessible from a lab test, which is sampled on a day scale. For control purposes, the correlations between the pulp properties and handsheet properties are established for feedback and therefore guide the process operating conditions. In this study, the bulk and tensile indices are selected as two important handsheet properties for modelling.

2.3 Process modelling

The CTMP process is complicated due to its time-varying and nonlinear behaviour. The energy to pulp quality transformation and the fibre development mechanisms are still not fully understood because of the complexities in its dynamics[29]. This causes the first-principle modelling of a CTMP process quite challenging. In this paper, to evaluate the refining process operation performance, two types of empirical models are developed and updated over time to capture the process variations. The established models are validated on the actual CTMP mill data set and achieved satisfactory accuracy, as illustrated in section 5.1. For the theoretical part of modelling, details are included in the subsequent sub-sections.

2.3.1 Pulp property modelling

Modelling is the most fundamental step for process operation evaluation. Models with simple structures are usually much easier and more robust for real-time implementation and maintenance compared with models in complicated structures. Many models designed for multivariate process control have been reported in the existing literature[3, 8, 26]. However, these models consider many refiner design parameters that are unavailable in the practical study necessitating to development of new models to describe the CTMP process. As a result, the autoregressive with exogenous input (ARX) model structure considering first-principles knowledge is employed to model the pulp freeness and shives.

From the previous pulp property modelling work[26], the pulp freeness and shives are mainly decided by the specific energy $E_{1:2}$, refining intensity $I_{1:2}$ and specific refining power $se_{1:2}$. The governing equations are as follows.

$$\begin{aligned} F_i &= (F_{i0} - k_1(E_i - E_{i0})) \cdot 10^{k_2(I_i - I_{i0})} \\ SC_i &= SC_{i0} \cdot 10^{k_3(E_i - E_{i0}) + k_4(se_i - se_{i0})} \\ se_i &= k_5 \cdot I_i \\ I_i &= \frac{E_i}{k_5 \cdot \tau}, \end{aligned} \quad , \qquad i = 1, 2 \tag{3}$$

where F_{i0} and SC_{i0} are the initial values of pulp freeness and shive content, respectively; E_{i0}, I_{i0} and se_{i0} denote the initial values of specific energy, refining intensity and specific refining power, respectively. $k_{1:5}$ are the refiner designing parameters, and the residence time τ denotes the duration that pulp passes through the refining zone, which is a function of refining consistencies $C_{1:2}$.

Moreover, the production rate, chemical add rate and chip preheater pressure are also considered during modelling as they impact the pulp qualities. In summary, integrating the empirical modelling in equation (3) and the other influential variables, the ARX models used in this paper are formulated as below:

$$\begin{aligned} F_t &= \phi_{t-d_k} \cdot \theta_{1,t} + w_t \\ \log(S_t) &= \phi_{t-d_k} \cdot \theta_{2,t} + v_t \\ \phi_{t-d_k} &= [F_{t-1} \ \cdots \ F_{t-n_a} \ \log(S_{t-1}) \ \cdots \ \log(S_{t-n_a}) \ \boldsymbol{u}_{t-d_k} \ \cdots \ \boldsymbol{u}_{t-d_k-n_b}] \end{aligned} \quad , \qquad t = 1, 2, \cdots, T \tag{4}$$

where the input vector $\boldsymbol{u}$ in the predictor ϕ is composed of $[P_r,\ r_c,\ P,\ C_1E_1,\ C_2E_2]$. $\log(\cdot)$ represents the logarithm operation with base 10, which is consistent with the shive content modelling in equation (3). $\theta_{1,t}$ and $\theta_{2,t}$ are the model parameters which are estimated and updated using the moving window least squares approach with unit stride. w_t and v_t are white Gaussian noise in the ARX models.

More specifically, the refining consistencies $C_{1:2}$ are included in this modelling as nonlinear features to determine the specific energy efficiency. From empirical study[30], for a given specific energy, different consistencies in the refining zone majorly influence the pulp quality. Therefore, a product of consistency and specific energy has been selected to model the impact of consistency on specific energy efficiency. $C_{1:2}$ cannot be measured online; therefore, the following models are employed to estimate $C_{1:2}$ online based on the dilution flow rate measurements[8].

$$\begin{aligned} C_1 &= \frac{100P_r}{P_r + k_d f_1 - k_{m1} M_1} \\ C_2 &= \frac{100P_r}{P_r/(0.01C_1) + k_d f_2 - k_{m2} M_2} \end{aligned} \tag{5}$$

where k_d, k_{m1}, k_{m2} are the process relevant model parameters, which are determined by matching the estimated consistency values to the lab consistency measurements.

Based on this modelling, the variations of freeness and shives can be precisely captured over time. Therefore, the real-time impacts of operating conditions on the pulp properties can also be evaluated.

Due to the complexity of the CTMP processes, model uncertainties, and system disturbances are crucial factors to consider. Considering the computational capability and available process information, this work adopts the adaptive ARX modelling strategy to model the system in real-time. However, it should be noted that to make the process model more robust to process disturbances and model uncertainties, more advanced modelling algorithms can be employed. The proposed framework has sufficient flexibility to embed different types of models.

2.3.2 Handsheet property modelling

Different from the pulp property modelling, the handsheet properties are accessible only from lab analysis with a very slow sampling rate. The built model is expected to provide a real-time

estimation of the selected handsheet properties, so that the desired pulp properties can be inferred from the designated handsheet qualities. Existing works mainly focus on building multivariate linear regression models to describe the correlations between pulp properties (such as freeness, shive contents and long fibre contents), and the handsheet properties (such as drainage time, burst, tear, bulk, etc.)[31, 32, 33]. In this work, after referring to the existing empirical models and conducting several tests on the actual mill data, a PLS regression model is employed for handsheet property modelling.

$$\begin{aligned} X_p &= T_p P_p^T + E_p \\ Y_h &= U_h Q_h^T + F_h \\ X_p &= [\boldsymbol{u}_{sc}\ \boldsymbol{u}_t\ \boldsymbol{u}_b\ \boldsymbol{u}_f\ \boldsymbol{u}_{P_r}] \in \mathcal{R}^{N \times m_x} \\ Y_h &= [\boldsymbol{y}^t\ \boldsymbol{y}^b] \in \mathcal{R}^{N \times m_y} \end{aligned} \tag{6}$$

where X_p and Y_h are the independent and dependent variables in this model, respectively; N, m_x and m_y denote the number of samples, input space dimension and output space dimension, respectively; E_p and F_h represent the measurement noise. The $\boldsymbol{u}$ and $\boldsymbol{y}$ components in X_p and Y_h are formulated as

$$\begin{aligned} \boldsymbol{u}_{sc} &= [\log(SC_1+1)\ \log(SC_2+1)\ \cdots\ \log(SC_n+1)\ \cdots\ \log(SC_N+1)]^T \\ \boldsymbol{u}_t &= [T_1\ T_2\ \cdots\ T_n\ \cdots\ T_N]^T \\ \boldsymbol{u}_b &= [B_1\ B_2\ \cdots\ B_n\ \cdots\ B_N]^T \\ \boldsymbol{u}_f &= [F_{2-\lambda_1}\ F_{3-\lambda_1}\ \cdots\ F_{n+1-\lambda_1}\ \cdots\ F_{N+1-\lambda_1}]^T \\ \boldsymbol{u}_{P_r} &= [P_{r,2-\lambda_2}\ P_{r,3-\lambda_2}\ \cdots\ P_{r,n+1-\lambda_2}\ \cdots\ P_{r,N+1-\lambda_2}]^T \\ \boldsymbol{y}^t &= [T_2\ T_3\ \cdots\ T_{n+1}\ \cdots\ T_{N+1}]^T \\ \boldsymbol{y}^b &= [B_2\ B_3\ \cdots\ B_{n+1}\ \cdots\ B_{N+1}]^T \end{aligned} \tag{7}$$

where F and P_r are sampled much faster than the handsheet properties, therefore the delay factors λ_1 and λ_2 are introduced to represent the sampling instants of F and P_r, particularly.

In equation (6), the factor and loading matrices T_p, U_h, P_p and Q_h are obtained by iterative decomposition[34]. The prediction of handsheet properties is performed through the multivariate

regression model $\hat{Y} = X \cdot B_p$, where B_p is calculated by the decomposed matrices in PLS regression[34].

3 CTMP process operation evaluation – A visualization approach

Among the CTMP process operation components in Fig. 1, the two-stage high consistency refining process is the most energy-intensive, and the power consumed by the refiners take approximately 80% of the entire mill total energy consumption, but with low efficiency[35]. As a result, much research has been done on the total specific energy optimization of pulp refining processes. These optimization strategies usually provide an optimum solution to the controllers, which operate the refining process automatically. However, in this work, the lack of stabilizing controller units in the actual CTMP process limits the realization of conventional optimization strategies. Therefore, inspired by the feasible region exploration in optimization, we developed a predictive operation performance evaluator to identify potential operation improvement and energy reduction opportunities. The feasible region of specific energies is comprehensively explored, and the evaluation results are visualized in real-time for further decision-making.

3.1 Proposed methodology overview

The challenges of process operation evaluation are manifold. The first challenge is determining specific evaluation metrics to assess the real-time operation performance. In the CTMP process under study, because the pulp properties suffer from significant variations, the operation performance cannot be determined solely by the currently produced pulp qualities, but also need to consider how likely a process can generate pulps with qualified properties. In addition, the second challenge arises when considering the measurement of impacts from selected process variables on the process operation. The third challenge occurs when evaluating high-dimensional variables systematically, including both inputs and outputs.

To properly address these challenges, a series of visualization and analysis units are established and illustrated in Fig. 3. Based on the pulp property model in equation (4), the impacts from process operating conditions to the pulp freeness and shives can be quantified. In order to facilitate the integration of multidimensional input and output variables, the Kiviat diagram[36] and a simply designed pulp quality classifier are employed to compress the multivariate inputs and outputs to

a visible dimension. From empirical process operations, the total specific energy consumption and its allocation to the two-stage refiners are core decision process variables, where the relationships $E_1 = TSE \cdot \alpha$ and $E_2 = TSE \cdot (1 - \alpha)$ hold. Meanwhile, since the potential of energy reduction is also a vital consideration of this study, among all the model input variables, TSE and α are selected as free variables to explore the feasible region and generate the predictive feasible map. The fixed process variables can affect the distribution of a feasible map and can also be involved in the free process variable set if needed. The generated feasible map is updated when new process measurements are available and provide statistics predicting the process operating status in the next sampling instant. The contribution generator block computes the contributions from both fixed and free process variables to the process operation. In the following subsections, the main functional blocks of the proposed methodology are introduced providing more details.

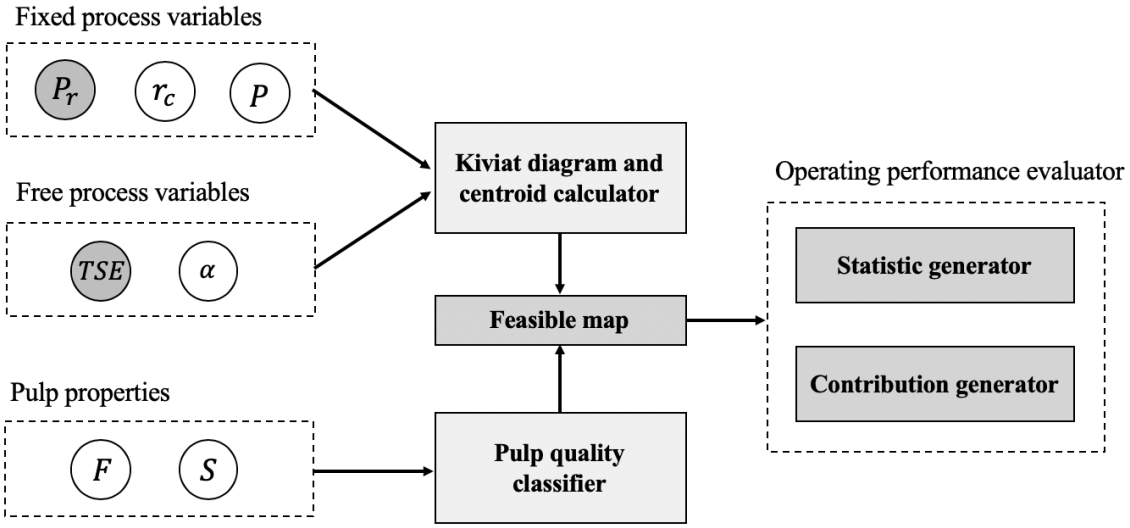

Figure 3: The schematic of the proposed operation performance visualization methodology, with shaded nodes representing OVs

3.2 Compressed visualization of process operating conditions and pulp properties

To compress the multidimensional process operating conditions and pulp properties for clear visualization, different strategies are adopted. Motivated by the time-explicit Kiviat diagram[37], the polar coordinate representation and the centroid calculation strategy are used to illustrate the

location of specific process operating conditions. On the other hand, the pulp properties are encoded by an empirical classifier with colored quality regions, as indicated in the pulp quality classifier block of Fig. 3.

3.2.1 Visualization of process operating conditions

To comprehensively explore the energy feasible region at a specific sampling instant t, the integrated process operating conditions are defined as

$$\boldsymbol{O} = \begin{bmatrix} TSE_1 & \alpha_1 & P_{r,t} & r_{c,t} & P_t \\ TSE_2 & \alpha_2 & P_{r,t} & r_{c,t} & P_t \\ \vdots & \vdots & \vdots & \vdots & \\ TSE_{N_s} & \alpha_{N_s} & P_{r,t} & r_{c,t} & P_t \end{bmatrix} = \begin{bmatrix} O_1 \\ O_2 \\ \vdots \\ O_{N_s} \end{bmatrix} \in \mathcal{R}^{N_s \times m_s} \tag{8}$$

where O represents the operating conditions regression matrix, $TSE_{1:N_s}$ and $\alpha_{1:N_s}$ denote the random sample pairs of the free process variables, with N_s samples in total. $P_{r,t}$, $r_{c,t}$ and P_t are consistent to the actual process operations at time t, which could affect the energy efficiency. m_s is the total number of selected MVs and OVs.

Not limited to the variable dimensions, the polar coordinate system allows us to represent one normalized sample vector in 2D space. For example, the sub-figures (a) and (b) in Fig. 4 illustrate how one sample and multiple samples are depicted in the polar coordinate system, where the process variables are aligned radially according to the designated angles with normalized magnitude values. Following this way, each sample vector O_{n_s} is presented as a closed polygon. To further simplify the illustration, the geometric center of each polygon is computed by converting the vertices of this polygon into 2D Cartesian coordinates and performing an average, as shown in equation (9).

$$\begin{aligned} x_{c,n_s} &= \frac{\sum_{i=1}^{m_s} x_{i,n_s}}{m_s} \\ y_{c,n_s} &= \frac{\sum_{i=1}^{m_s} y_{i,n_s}}{m_s} \end{aligned} \tag{9}$$

where the pair (x_{i,n_s}, y_{i,n_s}) denotes the Cartesian coordinate of the i^{th} vertex or process variables, and (x_{c,n_s}, y_{c,n_s}) denotes the computed centroid coordinate.

As a result, each multivariate sample O_{n_s} is compressed as a centroid point (x_{c,n_s}, y_{c,n_s}), as

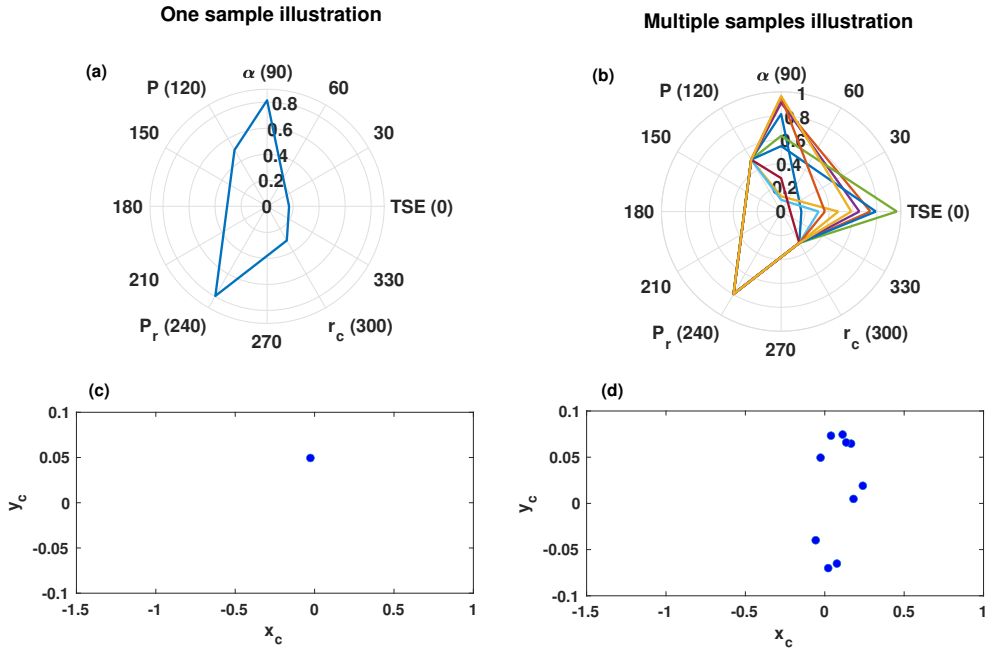

Figure 4: The illustration of one sample and multiple samples in polar coordinate system (subfigures (a) and (b)) and their corresponding centroids in 2D Cartesian coordinate system (subfigures (c) and (d))

illustrated in the sub-figures (c) and (d) of Fig. 4. This approach achieves the visualization of process operating conditions, and the visualization of pulp properties is explained in the next subsection.

3.2.2 Visualization of pulp properties

The evaluation of pulp properties mainly focuses on how desired or undesired the pulp qualities are. Therefore, an encoder is needed to convert the pulp property measurements into different production levels, which is denoted as the pulp quality classifier. In this work, benefiting from the two-dimensional pulp properties, the linear separator is employed for quality region segmentation based on the mill requirements after assessing the handsheet properties. Fig. 5 shows the segmentation of pulp freeness and shives. From mill production requirement, the pulp freeness should be bounded within the freeness upper and lower bounds, and pulp shives should be constrained below the shives upper bound, as shown in the green region of Fig. 5. For instance, region 2 (red) and region 3 (yellow) represent freeness degradation and shive degradation, respectively, and the

underlying causes and solutions should be figured out independently. Such color annotation leads to a differentiable pulp quality visualization, which can be integrated with the operating condition visualization to create feasible maps.

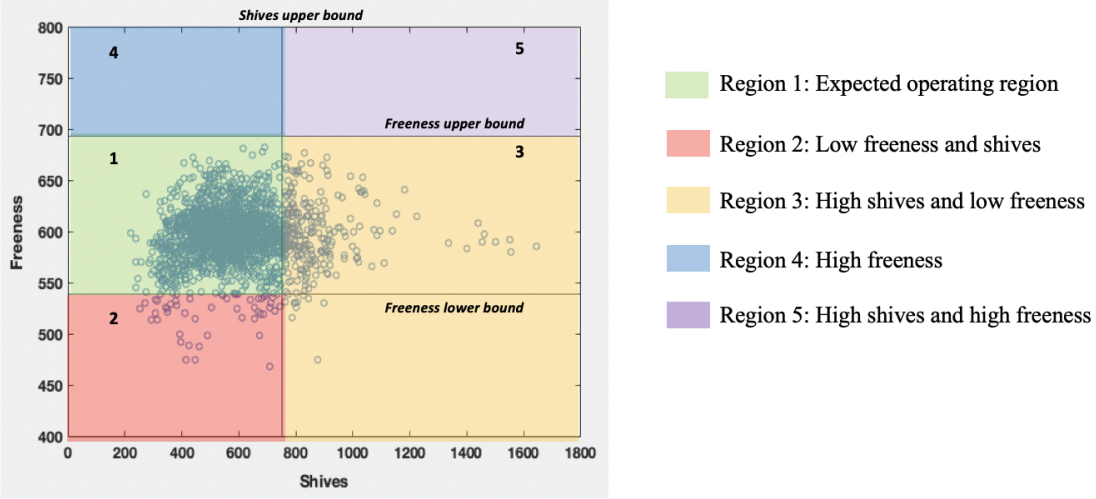

Figure 5: The pulp property segmentation

3.3 Feasible map creation and analysis

The feasible map is built based on linking and visualizing the explored feasible process operating region and the predicted pulp quality regions. The feasible map is updated as and when the process model, MVs, and OVs change over time. Fig. 6 contains a snapshot of the generated feasible map on 15-Jan-2021 at 19:00:00, where the process operating conditions are represented by their corresponding centroids. Each color represents one pulp quality level. The feasible map displays as many explorations and performances as possible, among which only one realization can happen in reality, as denoted by the ♦ in Fig. 6. At the sampling instant $t-1$, the feasible map works as a predictor and evaluator for the process operation decision at time t, where the validation is performed using actual process measurements simultaneously.

By creating a feasible map, some information about real-time process operations can be derived. Firstly, we can observe the impacts of fixed process variables on energy efficiency. In an extreme situation, if one set of fixed process variables can make 100% reproductions falling into green regions, then this process has a higher possibility to provide satisfied pulp products than the one with 0%

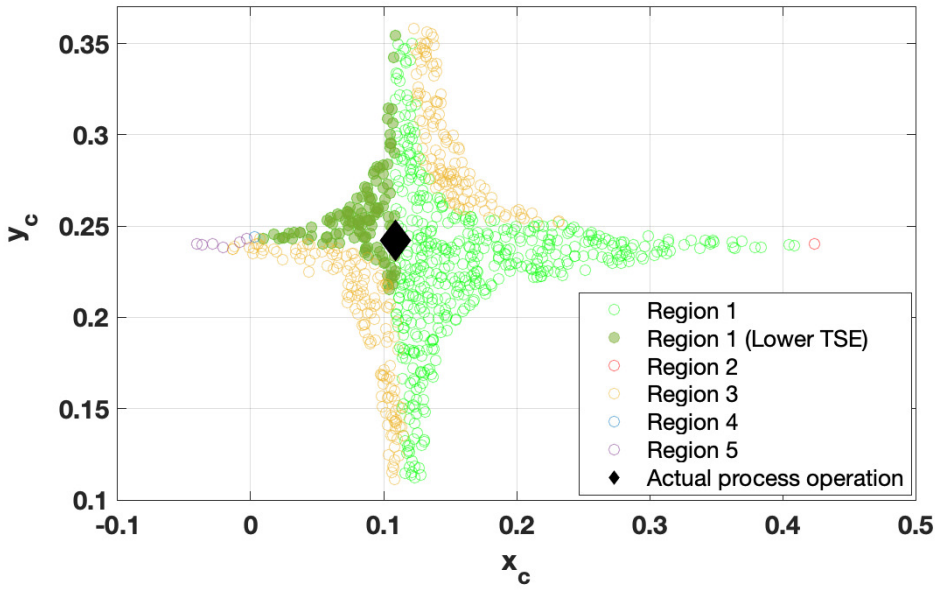

Figure 6: The feasible map generated to evaluate the process operation on 15-Jan-2021 at 19:00:00

green region partition. Therefore, the quality region distribution can be claimed as a good indicator for process operation evaluation. Secondly, comparing the energy exploration and the actual energy consumption, the potential energy-saving operation areas can be figured out, as illustrated in the shaded green region of Fig. 6. Finally, by tracking the movements of process variables and the feasible map in real-time, the causes of performance improvement or degradation can be diagnosed.

As a summary, the statistics listed in Table 2 can be used to evaluate the process operations and compute potentially reduced energy consumption. The contribution indices in Table 2 are used to calculate the contribution from the i^{th} process variable PV_i to the quality region distribution in the feasible map from time $t-1$ to t. The transition probabilities $P(I_t = 1|I_{t-1} = k_1, \delta(PV_i))$ and $P(I_t = k_2|I_{t-1} = 1, \delta(PV_i))$ represent the increment and loss of the good quality region, respectively, where I_t denotes the pulp quality region at time t and $\delta(PV_i)$ is computed by comparing the effect of PV_i at time t and time $t-1$. The weights w_{k_1} and w_{k_2} are pre-defined according to the actual process requirement.

Table 2: Summary of the statistics and contribution indices from the feasible map

Statistics	Formulation	Description
Quality region distribution	$p_j = \frac{N_j}{\sum_{j=1}^{n_r} N_j},\ j = 1, \cdots, n_r$ N_j - the number of samples in the j^{th} region n_r - the total pulp quality region number	Represent how likely a process is able to provide pulp with desired quality
Potential energy saving	$r_{TSE} = \frac{TSE_a - median(TSE_p)}{TSE_a}$ TSE_a - the actual TSE TSE_p - the potential reduced TSEs	Represent the potential percentage of total specific energy saving
Contribution indices	**Formulation**	**Description**
Contribution of the i^{th} process variable at time t	$l_{i,t} = \sum_{k_1=2}^{n_r} w_{k_1} l_{i,t}^{(k_1)} - \sum_{k_2=2}^{n_r} w_{k_2} l_{i,t}^{(k_2)}$ $l_{i,t}^{(k_1)} = P(I_t = 1 \mid I_{t-1} = k_1, \delta(PV_i)),\ k_1 = 2, \cdots, n_r$ $l_{i,t}^{(k_2)} = P(I_t = k_2 \mid I_{t-1} = 1, \delta(PV_i)),\ k_2 = 2, \cdots, n_r$	Calculate the quality region transition caused by the variation of PV_i

4 Handsheet property model reliability analysis

In section 2.3.2, we have presented the predictive inferential sensor modelling of the handsheet properties. The estimated inferential sensor model is used to generate the estimated handsheet properties with a faster sampling rate and can be employed to guide process operations by setting the desirable pulp properties. Because of the infrequent update and long-time usage, the reliability evaluation of the inferential sensor model is critical and can be achieved by characterizing the correlation between the input operating space and the model prediction error. During the model training period, the collected historical input data might not be uniformly sampled. Therefore, observing increased model uncertainties in specific input operating spaces is natural.

In order to quantify the model reliability, the relationship between the model input and model prediction error is established based on the model training performance. Considering the model in equation (6), its corresponding reliability level can be categorized into binary classes as follows:

$$r^b = \begin{cases} 0 \text{ (High reliability level)} & \text{if } |e^b| \leq th^b \\ 1 \text{ (Low reliability level)} & \text{otherwise} \end{cases} \tag{10}$$

where r^b represents the reliability level of the bulk model; $e^b = y^b - \hat{y^b}$ denotes the bulk model prediction error, with threshold th^b defined according to the empirical requirement of the model accuracy.

As a result, during online implementation, for a given new fast sampling input vector $u^r_{new} = [u_{f,new}\ u_{P_r,new}]$, the first objective is to identify the corresponding reliability level based on historical training data as below:

$$r^b_{new} = \underset{r^b}{\operatorname{argmax}}\, P(r^b | u^r_{new}; \hat{\mu^b_0}, \hat{\Sigma^b_0}, \hat{\mu^b_1}, \hat{\Sigma^b_1}, \hat{p^b_0}) \tag{11}$$

where the set $\{\hat{\mu^b_{0:1}}, \hat{\Sigma^b_{0:1}}\}$ includes all the probabilistic classifier parameters identified from historical training data, and $\hat{p^b_0}$ denotes the estimated prior probability of defining a high reliable bulk model without any observation. These parameters are estimated by maximizing the following likelihood function.

$$\{\hat{\mu^b_{0:1}}, \hat{\Sigma^b_{0:1}}, \hat{p^b_0}\} = \underset{\mu^b_{0:1}, \Sigma^b_{0:1}, p^b_0}{\operatorname{argmax}} \sum_{n_c \in N_c} \log\{P(u_{f,n_c}, u_{P_r,n_c} | r^b_{n_c}; \mu^b_{r^b_{nc}}, \Sigma^b_{r^b_{nc}}) \cdot P(r^b_{n_c}; p^b_0)\} \tag{12}$$

where the input vector $[u_{f,n_c}\ u_{P_r,n_c}]$ is assumed to follow different multivariate Gaussian distributions parameterized by mean vector μ and covariance matrix Σ under different conditions, such as, $r^b_n = 0, 1$. N_c is created by selecting the training samples whose Euclidean distances to the new input u^r_{new} are less than the Euclidean distance median of all the training samples.

Therefore, the posterior probability in equation (11) is computed as

$$P(r^b = j | u^r_{new}; \hat{\mu^b_0}, \hat{\Sigma^b_0}, \hat{\mu^b_1}, \hat{\Sigma^b_1}, \hat{p^b_0}) = \frac{P(u^r_{new} | r^b = j; \hat{\mu^b_j}, \hat{\Sigma^b_j}) \cdot P(r^b = j; \hat{p^b_0})}{\sum_{i=0}^{1} P(u^r_{new} | r^b = i; \hat{\mu^b_i}, \hat{\Sigma^b_i}) \cdot P(r^b = i; \hat{p^b_0})}, \qquad j = 0, 1 \tag{13}$$

So far, a new input sample's reliability level is completely defined by its neighbours' reliability levels in the model training data set. However, such classification does not consider the spatial distributions between the new sample and its adjacent training samples. This conclusion arises from the uncertainty of the underlying distribution $u^r_{new} | r_{new} \sim \mathcal{N}(\mu_{r_{new}}, \Sigma_{r_{new}})$, which might not be fully consistent to the distribution $u_{N_c} | r_{N_c} \sim \mathcal{N}(\mu_{r_{N_c}}, \Sigma_{r_{N_c}})$ of the adjacent training samples. Therefore, a Gaussian process model[38] is employed to evaluate such uncertainty. The final reliability index is created by integrating both the Gaussian process model output and the reliability classifier output.

A Gaussian process model is created by extending the conventional multivariate Gaussian distri-

bution to an infinite dimensional stochastic process[39]. In our work, we use a Gaussian process prior to modelling the prior distribution of prediction error with respect to the input space, as below.

$$e^b(u) \sim \mathcal{GP}(m(u), k(u, u')) \tag{14}$$

where $m(u)$ and $k(u, u')$ are Gaussian process prior mean and covariance functions, respectively, and u denotes any arbitrary input sample within the input sample space. For simplicity, in this work, $m(u) = 0$ is chosen as the prior mean, and the widely used kernel formulation is employed to represent $k(u, u')$ as follows:

$$k(u_i, u_j) = \exp(-\frac{1}{2\delta^2}||u_i - u_j||) \tag{15}$$

where δ is the hyper parameter controlling the width of the kernel and $||\cdot||$ indicates the Euclidean distance calculator.

By means of such prior distribution, given input value u_s, we can infer the prediction error posterior probability distribution $e^b(u_s)|\{u_{f,n}, u_{P_r,n}, e^b_n\}_{n=1}^N, u_s \sim \mathcal{N}(\mu_s(u_s), \sigma_s^2(u_s))$ by using Sherman-Morrison-Woodbury formula[40]. The posterior mean and covariance functions $\mu_s(u_s)$ and $\sigma_s^2(u_s)$ are in the following formulations.

$$\begin{aligned} \mu_s(u_s) &= \boldsymbol{k}\boldsymbol{K}^{-1}[e^b_1 \ e^b_2 \ \cdots \ e^b_N]^T \\ \sigma_s^2(u_s) &= k(u_s, u_s) - \boldsymbol{k}\boldsymbol{K}^{-1}\boldsymbol{k}^T \end{aligned} \tag{16}$$

where the kernel vector $\boldsymbol{k}$ and kernel matrix $\boldsymbol{K}$ are

$$\begin{aligned} \boldsymbol{k} &= [k(u_s, [u_{f,1}, u_{P_r,1}]) \ k(u_s, [u_{f,2}, u_{P_r,2}]) \ \cdots \ k(u_s, [u_{f,N}, u_{P_r,N}])] \in \mathcal{R}^{1\times N} \\ \boldsymbol{K} &= \begin{bmatrix} k([u_{f,1}, u_{P_r,1}], [u_{f,1}, u_{P_r,1}]) & \cdots & k([u_{f,1}, u_{P_r,1}], [u_{f,N}, u_{P_r,N}]) \\ \vdots & \vdots & \vdots \\ k([u_{f,N}, u_{P_r,N}], [u_{f,1}, u_{P_r,1}]) & \cdots & k([u_{f,N}, u_{P_r,N}], [u_{f,N}, u_{P_r,N}]) \end{bmatrix} \in \mathcal{R}^{N\times N} \end{aligned} \tag{17}$$

Hence, the formulation of the reliability index for any arbitrarily defined input sample u_s is

$$\begin{aligned} RI(u_s) = P(e^b(u_s) \le th^b | u_s, \{u_{f,n}, u_{P_r,n}, e^b_n\}_{n=1}^N) \cdot P(r^b_{u_s} = 0 | u_s, \hat{\mu^b_0}, \hat{\Sigma^b_0}, \hat{\mu^b_1}, \hat{\Sigma^b_1}, \hat{p^b_0}) \\ -P(e^b(u_s) > th^b | u_s, \{u_{f,n}, u_{P_r,n}, e^b_n\}_{n=1}^N) \cdot P(r^b_{u_s} = 1 | u_s, \hat{\mu^b_0}, \hat{\Sigma^b_0}, \hat{\mu^b_1}, \hat{\Sigma^b_1}, \hat{p^b_0}) \end{aligned} \tag{18}$$

where the probability $P(e^b(u_s) \leq th^b|u_s, \{u_{f,n}, u_{P_r,n}, e_n^b\}_{n=1}^N)$ is computed by the Gaussian process posterior and $P(r_{u_s}^b = 0|u_s, \hat{\mu_0^b}, \hat{\Sigma_0^b}, \hat{\mu_1^b}, \hat{\Sigma_1^b}, \hat{p_0^b})$ is calculated by the reliability level classifier in equation (13).

The point to be noted here is that even though the Gaussian process posterior can reflect the prediction error distribution of any given u_s, it is still insufficient to be used independently for model reliability evaluation. That is because the Gaussian process model can only provide a rough estimation of the prediction errors. But on the other hand, such estimation can offer a good measurement of the error distribution uncertainty from the covariance function $\sigma_s^2(u_s)$. In equation (18), only when both the Gaussian process model and reliability classifier confirm the high-reliability level, the reliability index RI will show a positive value. The larger RI implies higher reliability of the model predictions at a given input operating point, and vice-versa. Therefore, this RI can guide the setting of desirable production pulp properties.

5 Performance validation on a real CTMP process

In this section, the performance of the above-proposed methodology is validated on a practical CTMP process operated by the Taylor Pulp mill of Canfor company, located in British Columbia, Canada. The mill provided two sets of data for process operation evaluation, ranging from October 2019 to December 2019, and January 2021 to September 2021, respectively. For simplicity, in the subsequent contents, these two data sets are denoted as 2019 data and 2021 data separately. Moreover, another data set with a longer duration, from July 2018 to September 2021, was provided for handsheet properties modelling and reliability analysis. The mill generally targets to produce paper products with multiple grades. In this study, the process operations under research mainly focus on the paper products with two grades (thickness (μm)/grammage (g/m^2)), i.e., 350/75 grade and 400/70 grade. Different product grades determine different production requirements, namely, various desirable pulp properties. As a result, the designed operation evaluation approach should be adjustable to the switching of product grades, which is achieved by the adaptive modelling approach and the flexible pulp property segmentation. In the following sub-sections, the modelling performances of pulp properties and handsheet properties are first demonstrated, and subsequently, the real-time process operation evaluation is also validated. Finally, the model reliability analysis

of handsheet properties is conducted and tested on the bulk property.

5.1 Pulp property and handsheet property modelling performance validation

5.1.1 Pulp property model validation

The modelling of pulp properties, i.e., freeness and shives, has been thoroughly explained in section 2.3.1, where the ARX model structure in equation (4) is employed. In order to adapt to process variations, a fixed-length moving window is used to update the models at every sampling instant. The model update window length in both cases is set as 300 hours. From the PulpEye analysis system, the pulp property measurements are available every 30 minutes on average. The model in equation (4) is built up based on this slower sampling rate. Since the process operating variables are accessible at a faster sampling rate, the freeness and shives can be estimated from the faster-sampled process variables if needed. The developed ARX model has no identifiability issues because of the convex nature of objective function and the proper choice of input, and sampling rate leading to unique parameter estimation. Unified model orders n_a and n_b are chosen for both data sets with values 2 and 3, correspondingly. After implementing the modelling technique, the actual measured and predicted pulp properties are illustrated in Fig. 7, from which we can observe that the model predictions precisely track the actual measurements. More detailed validation statistics are included in Table 3, where the R value is calculated from the model prediction and actual measurement. When R is equal to 1, the measurement and prediction are perfectly matched, which is impossible due to noise contamination. From Table 3, the R values are as high as 0.9119 and 0.8828 for freeness and shives predictions, respectively. The normalized $RMSE$ values are as low as 0.0215 and 0.1232 for freeness and shives, respectively. Such model prediction accuracy is sufficient enough for process operation evaluation purposes.

Table 3: Pulp property model validation statistics

	2021 Case		2019 Case	
	R value	Normalized $RMSE$	R value	Normalized $RMSE$
Freeness	0.9119	0.0215	0.8537	0.0458
Shives	0.8137	0.1582	0.8828	0.1232

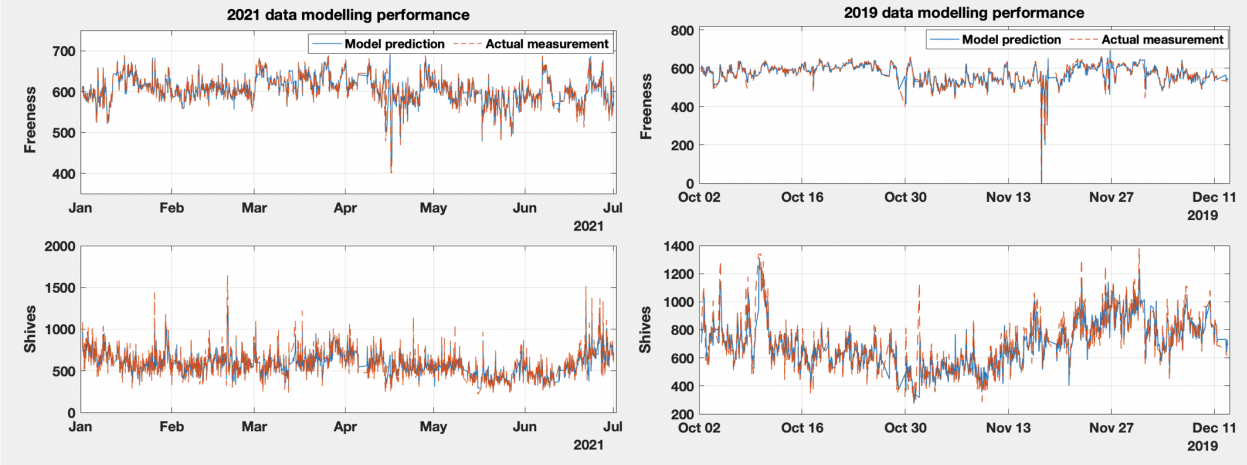

Figure 7: The pulp property modelling performance in 2019 and 2020 data sets

5.1.2 Handsheet property model validation

Following the handsheet property modelling described in section 2.3.2, we have integrated the relevant process variables and developed the PLS regression model formulated in equations (6) - (7). The previous lab measurements and frequently sampled variables are employed for future tensile and bulk predictions. Similar to the pulp property modelling, in order to accurately reflect the actual process responses, the handsheet property model is also updated using the moving window strategy over time with the model updated every sampling instant. The model update window length is selected as 100 samples in this scenario. Moreover, the handsheet property measurements are available at the frequency of one to two samples per day. The actual measurements of pulp properties are available every 30 minutes on average, and the process operating variables are accessible at a faster sampling rate every minute. The tensile and bulk modelling performance is illustrated in Fig. 8, where one can observe that the model predictions can capture the main trend of the actual measurements. In Table 4, the R values of the lower two sub-figures in Fig. 8 are computed as 0.7698 and 0.7059. Potential reasons for such deterioration include the extremely sparse and irregular lab samples available for modelling, and also, the model update is conducted relatively less frequently than the pulp properties. Compared to the existing literature[2], the computed R values and normalized $RMSE$ values imply a satisfactory performance of the identified handsheet property models.

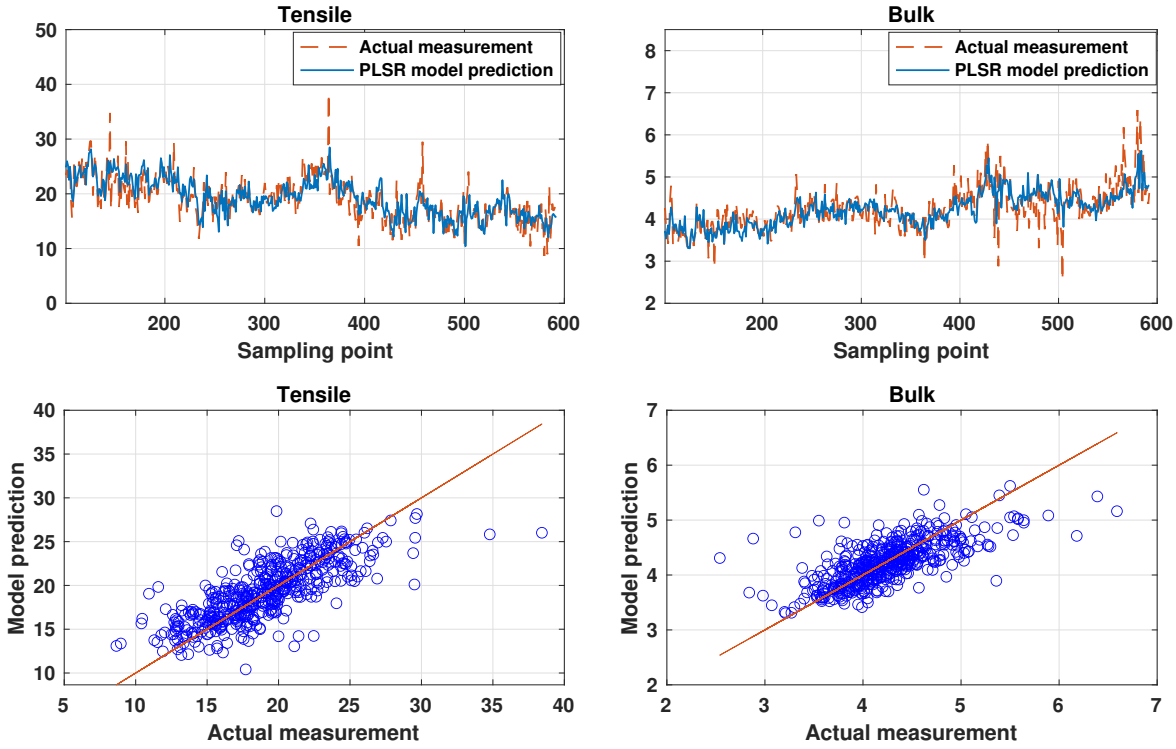

Figure 8: The handsheet property modelling performance

Table 4: Handsheet property model validation statistics

Tensile		Bulk	
R value	Normalized $RMSE$	R value	Normalized $RMSE$
0.7698	0.1328	0.7059	0.0682

5.2 Performance validation on the proposed real-time process operation evaluation approach

Following the proposed methodology described in section 3, the CTMP process operation can be evaluated in real-time based on the identified pulp property ARX models. Consistent with the modelling, the same operation duration in 2019 and 2021 has been employed for performance demonstration, during which the process operation is switched between two production grades, i.e., 400/70 and 350/75 grades. The preliminary configuration starts from segmenting the pulp quality regions, as shown in Fig. 5, by predetermining the freeness and shives bounds. So far, in accordance with the mill operation requirement, the bounds of freeness and shives under different product grades

are summarized in Table 5. After applying these requirements, the pulp quality classifier assorts every single pulp property output to one out of five quality regions. In summary, simple comparative statistics of pulp quality classifier outputs are integrated into Table 6, from which we can conclude that the process operation in 2021 is much better than that in 2019 with respect to the satisfaction of product requirements. In the next step, we presented an online predictive feasible map as introduced in section 3.3 at every sampling instant and validated its effectiveness using practical process data.

Table 5: Mill requirements on pulp property under different product grades

	350/75 grade		400/70 grade	
	Upper bound	Lower bound	Upper bound	Lower bound
Freeness	700	570	700	595
Shives	750	0	1000	0

Table 6: Pulp quality region distribution in 2019 and 2021 investigation

	Pulp quality region and distribution				
	Region 1 (Expected)	Region 2	Region 3	Region 4	Region 5
2019 operation	38.47%	36.18%	25.34%	0	0
2021 operation	80.46%	10.38%	9.17%	0	0

Referring to Table 2, the first set of information that is obtained from the predictive feasible map in Fig. 6 is the quality region distributions. Based on the obtained feasible map, the quality region distributions for both 2019 and 2021 case studies are shown in Fig. 9. Here, we can find major differences between the 2019 and 2021 quality region distributions, where the expected region 1 dominates the most operating time in 2021 but only occupies part of the operating time in 2019. This finding is consistent with the comparative performance illustrated in Table 6.

The advantage of the feasible map is its predictive capability; therefore, it can provide quality region distributions several minutes ahead of the actual event occurrence. In this way, the continuous degradation of region 1 or the increase of the other regions can alert the variations of the process, which might result in unsatisfied product qualities. Several thresholds ranging from 0.9 to 0.5 are selected as conditions to demonstrate the predictive accuracy to predict the most likely happened region in the upcoming sampling instant and compared it with the actual process outcome. Table 7 summarizes the test results in both the 2019 and 2021 case studies. In Table 7, the percentages corresponding to different regions are the prediction accuracy for both cases using different

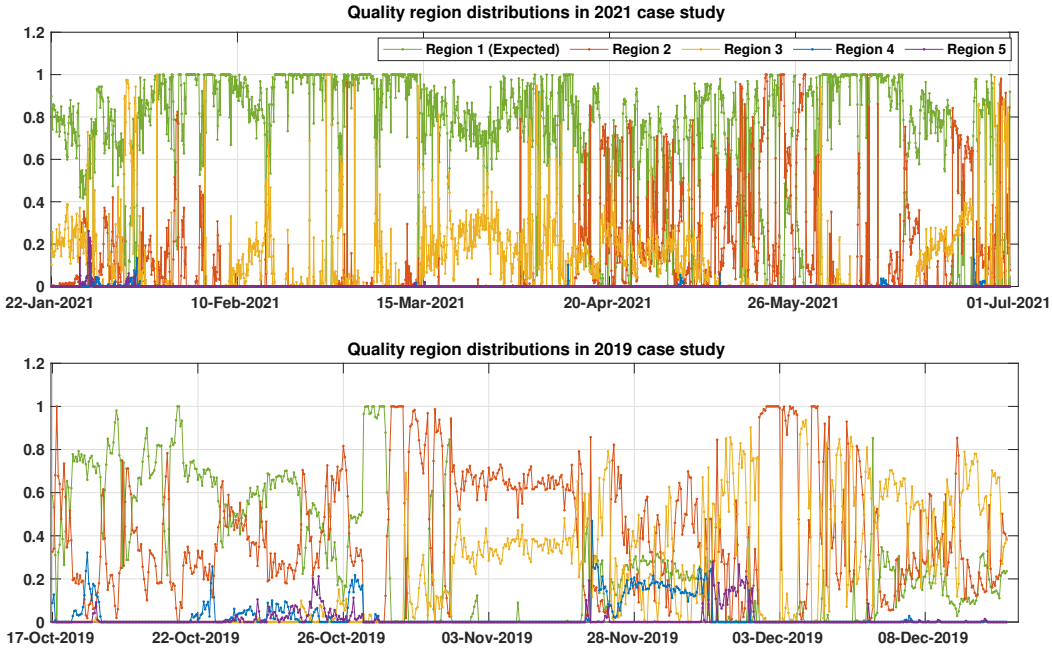

Figure 9: The comparison of quality region distributions in 2019 and 2021 case studies

thresholds. For example, when the threshold is selected as 0.9, the feasible map has more than 90% confidence to predict the next quality region, and the accuracy of such prediction is computed for all the regions. One can conclude from Table 7 that given threshold 0.9, the prediction accuracy of both 2019 and 2021 cases are the most accurate, while as the threshold decreases, the prediction accuracy gets decreased, which is natural as the feasible map confidence level also decreases. The last row of Table 7 summarizes the portion of data that has the outstanding region distribution. The higher portion value implies a wider feasible map. Note that the thresholds for different region predictions can be set differently for better prediction performance. In a real-time implementation, especially working with the complicated time-varying CTMP process, it is unrealistic to expect the proposed strategy to continually maintain close to 100% accuracy. Whenever the feasible map can provide high confidence in its prediction, the corresponding solutions can be considered to help improve the process operations.

Based on the evaluation statistics listed in Table 2, the process operation periods with potential energy-saving possibilities can be identified with energy reduction estimations. By setting the predictive threshold as 0.6 for the 2019 case study, 64.23% samples have more than 80% accurate

Table 7: Test performance of the feasible map predictive capability

Predictive Threshold	0.9		0.8		0.7		0.6		0.5	
	2019	2021	2019	2021	2019	2021	2019	2021	2019	2021
Region 1	100%	95.47%	95%	96.03%	94.94%	94.39%	93.43%	92.23%	91.57%	91.38%
Region 2	88.68%	90.32%	84.06%	83.64%	82.86%	77.45%	86.43%	70.18%	76.86%	68.63%
Region 3	100%	92.59%	88.24%	86.36%	81.40%	81.97%	81.40%	76.83%	80%	72.22%
Region 4	100%	100%	100%	100%	100%	100%	100%	100%	100%	100%
Region 5	100%	100%	100%	100%	100%	100%	100%	100%	100%	100%
Covered portion of all data	12.33%	38.12%	19.18%	57.37%	34.55%	76.24%	64.23%	89.67%	84.63%	96.75%

predictions in all the regions, which means the feasible map provides more reliable process operation evaluations than using a lower threshold, such as 0.5. Hence, the ratio of energy reduction is computed for these 64.23% samples and is illustrated in Fig. 10. In the 2021 case study, instead of using a unified threshold for all the regions, compound predictive thresholds are applied, with a threshold value of 0.8 for region 2 and 0.7 for the other regions. In this way, 73.62% samples are considered in the 2021 case for energy consumption evaluation. As illustrated in Fig. 10, the total specific energy can be reduced compared with actual process energy consumption, and the average energy reduction ratios for 2019 and 2021 are calculated as 6.40% and 7.92%, respectively. It is worth noting that the negative energy-saving ratios happening in the 2021 case study indicate the scenarios where more energy consumption is required to bring the process from the other region back to the expected quality region 1.

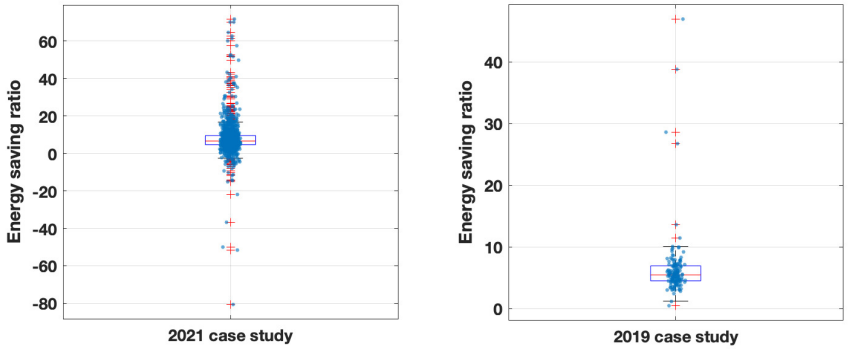

Figure 10: The energy saving ratios in 2019 and 2021 case studies

Finally, the last information derived from the predictive feasible map is the contribution indices of different process variables. In Fig. 11, the contribution indices and quality region distribution

from October 26, 2019 to October 28, 2019 are shown as an illustration, where one can observe the gradual variation of region distributions and the corresponding PV contributions. The positive and negative contributions reflect the process changes caused by the PV_i variations, and these contributions can be used to guide the process operations. In this particular case, the weights w_{k_1} and w_{k_2} remain the same for all quality region transitions, while they can also be adjusted individually to emphasize some especially desirable or undesirable quality region switches.

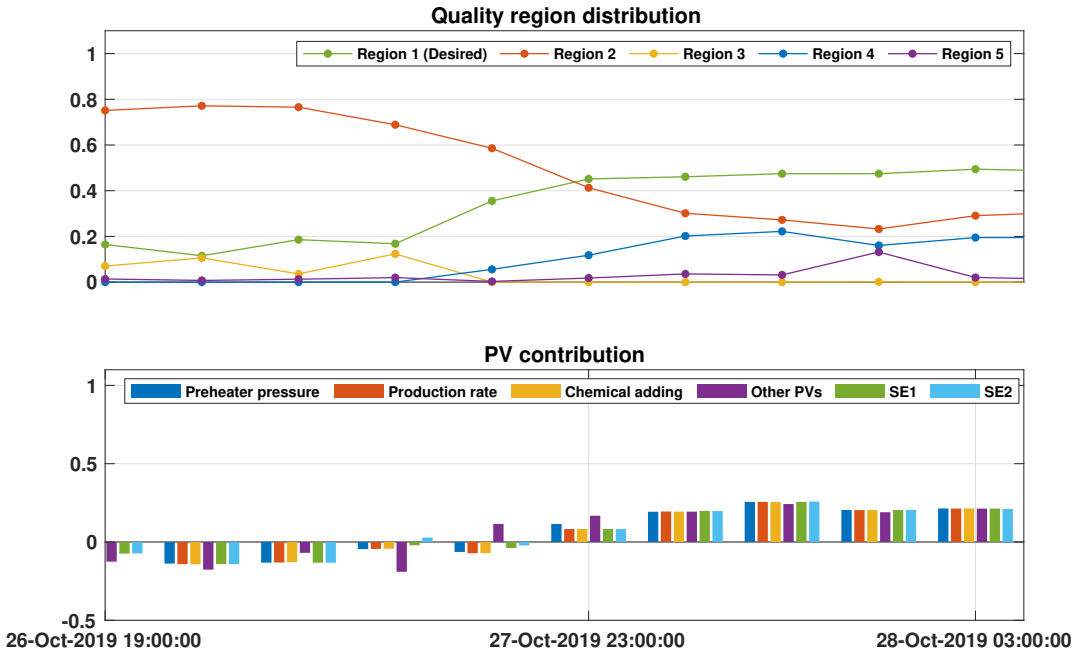

Figure 11: The illustrative snapshot of contribution indices from process variables

5.3 Performance validation on handsheet property model reliability analysis

In the above section 5.1.2, the tensile and bulk indices are modelled and the performance is illustrated in Fig. 8. Following the reliability analysis method introduced in section 4, the bulk model is selected to evaluate as it has a lower R value than the tensile model. First of all, the distribution of bulk model absolute prediction error is depicted in Fig. 12, where the threshold th^b of the model reliability level is selected as 0.4. From precise statistical analysis, for 79.88% instances, the bulk model generates predictions with a higher reliability level, and for 20.12% cases, the model

provides predictions with a lower reliability level. We aim to further evaluate the modelling reliability against the model input space.

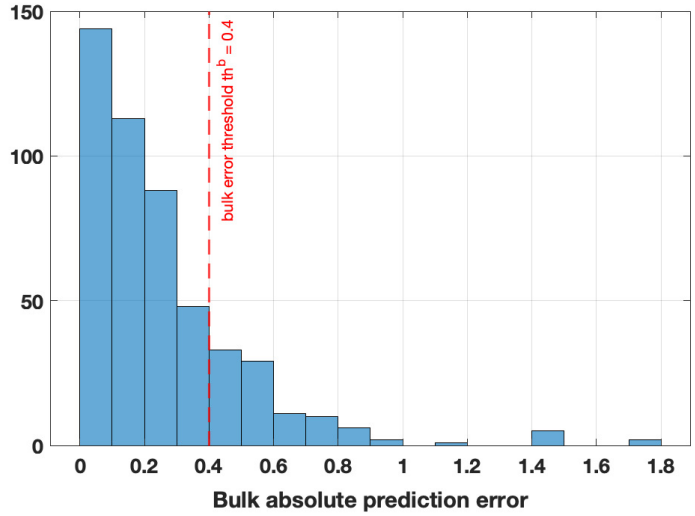

Figure 12: The distribution of bulk absolute prediction error

Because all the estimated models in this work are updated using the moving window strategy at every sampling instant, the model reliability classifier in equations (11) - (13) and the Gaussian process model in equations (14) - (17) are also evaluated whenever a new model is obtained from training data set. In this work, the free input space $[u_f, u_{P_r}]$ is two-dimensional; therefore, the illustrations of results are achievable. Taking the reliability analysis on the identified model on December 17, 2019, as an example, Fig. 13 includes the estimated posterior distribution $e^b(u_s)|\{u_{f,n}, u_{P_r,n}, e^b_n\}_{n=1}^N, u_s \sim \mathcal{N}(\mu_s(u_s), \sigma_s^2(u_s))$, where $\mu_s(u_s)$ and $\sigma_s^2(u_s)$ are depicted in the left and right sub-figures, respectively. The green and red dots are the model training samples labelled with $r^b = 0$ and $r^b = 1$, respectively. From this illustration, we can first find that this estimated posterior distribution can provide the mean value of $e^b(u_s)$ from the training data, and the sampling areas with denser red dots tend to generate higher absolute prediction errors. Also, in the $\sigma_s^2(u_s)$ illustration, the uncertainty of posterior estimation is also computed from the sampling density and the input space areas with fewer training samples have higher error uncertainty and will therefore be assigned with lower reliability index values.

After integrating the posterior error distribution and the reliability classifier outcome, the prob-

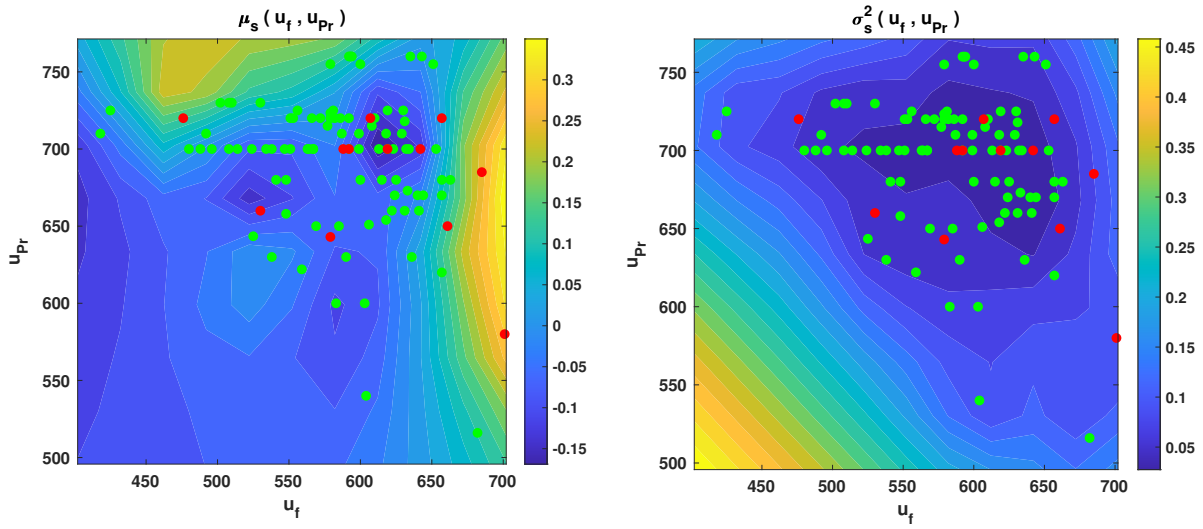

Figure 13: The illustration of bulk prediction error posterior distribution estimated from Gaussian process, with green dots and red dots representing the training samples with high-reliability levels and low-reliability levels, respectively.

ability of $r^b = 1$ and the reliability index RI in the input space are calculated and shown in Fig. 14. Here, from the estimation of $P(r^b = 1|u_f, u_{P_r}; \hat{\mu_{0:1}^b}, \hat{\Sigma_{0:1}^b}, \hat{p_0^b})$ in the left sub-figure, we can observe that certain areas which are rarely sampled could have a lower probability of $r^b = 1$ because the adjacent samples are more reliable. The RI integrates the classifier output and the estimated absolute error posterior distributions, resulting in different levels of reliability in the rarely sampled areas. The reliability index chart can help the operator define the desired pulp freeness given specific production rates. When testing the pulp freeness in the area with a higher RI value, the process operator can trust the handsheet property model.

Finally, as a comprehensive validation, we applied the model reliability index to estimate the reliability levels throughout the input space and validated our estimated result with the actual process measurement. Here, to provide a more conservative validation result, we set a threshold of 0.2 for RI, which means that if $RI > 0.2$, we claim that this input sample can provide prediction with a high-reliability level and vice-versa. The actual process measurement at the next sampling instant is applied to match and validate the reliability prediction. The validation results are summarized in Table 8. Here, for the cases with calculated $RI > 0.2$, there are more than 80% bulk predictions with smaller absolute prediction errors, and this portion is much more significant than the cases with computed $RI \leq 0.2$. On the other hand, when the estimated $RI \leq 0.2$, there are

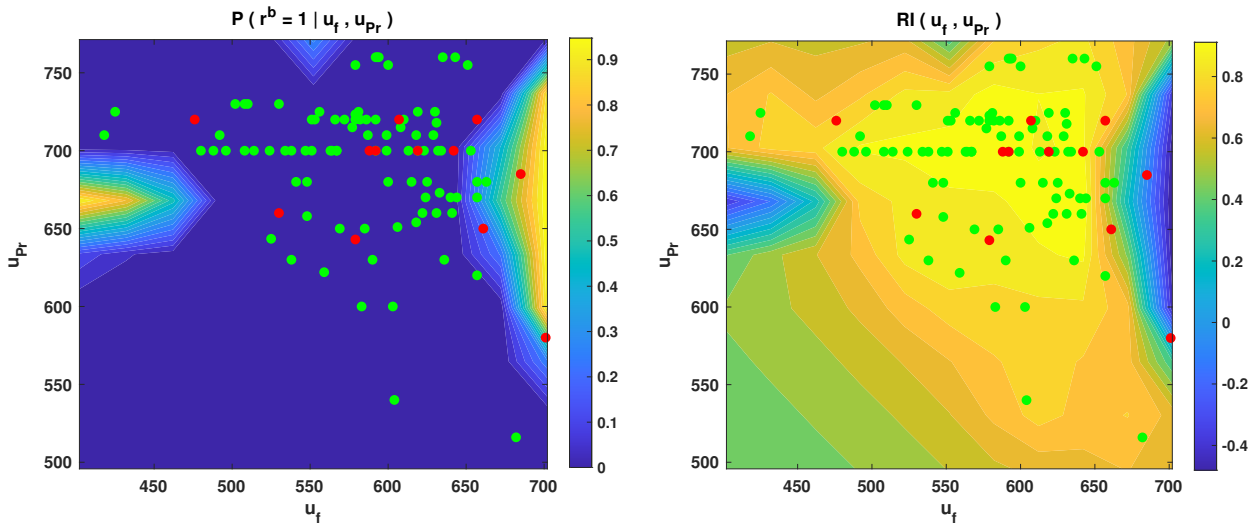

Figure 14: The illustration of reliability classifier outcome (left subfigure) and the reliability index (right subfigure), with green dots and red dots representing the training samples with high-reliability levels and low-reliability levels, respectively.

outstandingly larger portions of data with $0.4 < |e^b| < 0.5$ and $|e^b| \geq 0.5$ than the other case. This clearly demonstrates the effectiveness of the proposed reliability index. Sampling the freeness and production rate in the area with higher RI could be more likely to result in more reliable model predictions of handsheet properties.

Table 8: Validation performance on the reliability analysis

	Estimated reliability level	
	$RI > 0.2$ (High reliability level)	$RI \leq 0.2$ (Low reliability level)
Actual $\|e^b\| \leq 0.4$	81.12%	57.69%
Actual $0.4 < \|e^b\| < 0.5$	6.01%	19.23%
Actual $\|e^b\| \geq 0.5$	12.88%	23.08%

6 Conclusions and Future works

In the continuous CTMP process, aiming at improving energy efficiency and maintaining the produced pulp quality, we proposed a non-intrusive operating recommendation system with an extensible framework. In this system, a high-dimensional visualization technique based on the Kiviat diagram has been employed to integrate the multidimensional process operating space and the product quality so as to assess how the process is operated over time. For real-time implementation,

two critical points, i.e., simpleness and robustness, are fully considered in this work. Simple and robust model structures are employed with sufficient accuracy, and intuitive illustrations of the process operating conditions with comprehensible statistics are provided. The proposed work links the process operating space to the intermediate pulp properties, which are controlled to regulate the handsheet properties. To further investigate the relationship between pulp properties and the handsheet properties, an inferential sensor model was developed with a reliability index to indicate which input sample area is more likely to provide more accurate predictions. The effectiveness of the proposed methodologies has been validated using the data extracted from a real-time CTMP process. The Future scope of the proposed work is as follows:

1. To further improve the model robustness, additional mechanical properties and the process disturbances from feedstock, such as fiber heterogeneity, will be considered. Thus, more valuable insights into the CTMP process can be obtained, leading to better process operations. Considering first-principle and data-driven modelling strategies, a hybrid predictive model structure could describe the correlations between process operating conditions and paper mechanical properties. Combining reinforcement learning techniques with this hybrid model structure would enhance the model's accuracy and assist in making proper process operation decisions.

2. The investigated process operation areas will be extended to screening and rejecting refining segments and eventually develop a plant-wide process operation evaluation strategy.

7 Acknowledgements

Thanks to the operations team of Canfor Pulp for helping with the data collection.

References

1. Pratima Bajpai. *Biermann's Handbook of Pulp and Paper: Volume 1: Raw Material and Pulp Making.* Elsevier, 2018.

2. Xingsheng Qian. *Modelling and dynamic simulation of CTMP plant.* PhD thesis, University of British Columbia, 1996.

3. Hui Tian, Qiugang Lu, R Bhushan Gopaluni, Victor M Zavala, and James A Olson. An economic model predictive control framework for mechanical pulping processes. *Control Engineering Practice*, 85:100–109, 2019.

4. Hui Tian, Qiugang Lu, R Bhushan Gopaluni, and Victor M Zavala. Multiobjective economic model predictive control of mechanical pulping processes. In *2016 IEEE 55th Conference on Decision and Control (CDC)*, pages 4040–4045. IEEE, 2016.

5. Hui Tian, Qiugang Lu, R Bhushan Gopaluni, Victor M Zavala, and James A Olson. Economic nonlinear model predictive control for mechanical pulping processes. In *2016 American Control Conference (ACC)*, pages 1796–1801. IEEE, 2016.

6. Eranda Harinath, Lorenz T Biegler, and Guy A Dumont. Advanced step nonlinear model predictive control for two-stage thermo mechanical pulping processes. *IFAC Proceedings Volumes*, 44(1):3653–3658, 2011.

7. Eranda Harinath, LT Biegler, and Guy A Dumont. Predictive optimal control for thermo-mechanical pulping processes with multi-stage low consistency refining. *Journal of process control*, 23(7):1001–1011, 2013.

8. Eranda Harinath, LT Biegler, and Guy A Dumont. Control and optimization strategies for thermo-mechanical pulping processes: Nonlinear model predictive control. *Journal of Process Control*, 21(4):519–528, 2011.

9. David Di Ruscio. Model predictive control and identification: A linear state space model approach. In *Proceedings of the 36th IEEE Conference on Decision and Control*, volume 4, pages 3202–3209. IEEE, 1997.

10. Huaijing Du, GA Dumont, and Ye Fu. Nonlinear control of a wood chip refiner. In *Proceedings of International Conference on Control Applications*, pages 1065–1066. IEEE, 1995.

11. Hyun-Kyu Choi, Sang Hwan Son, and Joseph Sang-Il Kwon. Inferential model predictive control of continuous pulping under grade transition. *Industrial & Engineering Chemistry Research*, 60(9):3699–3710, 2021.

12. Anders Karlström, Karin Eriksson, David Sikter, and Mattias Gustavsson. Refining models for control purposes. *Nordic Pulp & Paper Research Journal*, 23(1):129–138, 2008.

13. Karin Eriksson and Anders Karlström. Mechanical pulping. *Nordic Pulp & Paper Research Journal*, 24(2):231–238, 2009.

14. Mehmet Mercangöz and Francis J Doyle III. Real-time optimization of the pulp mill benchmark problem. *Computers & Chemical Engineering*, 32(4-5):789–804, 2008.

15. Michael Elsinga. TMP optimization using multivariate analysis [thermo-mechanical pulp mill]. In *Conference Record of the 2002 Annual Pulp and Paper Industry Technical Conference (Cat. No. 02CH37352)*, pages 10–15. IEEE, 2002.

16. Wipawadee Nuengwang, Thongchai R Srinophakun, and Matthew J Realff. Real-time optimization of pulp mill operations with wood moisture content variation. *Processes*, 8(6):651, 2020.

17. Hyun-Kyu Choi and Joseph S-I Kwon. Multiscale modeling and multiobjective control of wood fiber morphology in batch pulp digester. *AIChE Journal*, 66(7):e16972, 2020.

18. Sunil Kumar Jauhar, Praveen Vijaya Raj Pushpa Raj, Sachin Kamble, Saurabh Pratap, Shivam Gupta, and Amine Belhadi. A deep learning-based approach for performance assessment and prediction: A case study of pulp and paper industries. *Annals of Operations Research*, pages 1–27, 2022.

19. B Talebjedi, T Laukkanen, H Holmberg, E Vakkilainen, and S Syri. Advanced energy-saving optimization strategy in thermo-mechanical pulping by machine learning approach. *Nordic Pulp & Paper Research Journal*, 37(3):434–452, 2022.

20. Hiromasa Kaneko, Masamoto Arakawa, and Kimito Funatsu. Applicability domains and accuracy of prediction of soft sensor models. *AIChE Journal*, 57(6):1506–1513, 2011.

21. Paul Nomikos and John F MacGregor. Multi-way partial least squares in monitoring batch processes. *Chemometrics and intelligent laboratory systems*, 30(1):97–108, 1995.

22. Hirokazu Kamohara, Akitoshi Takinami, Makoto Takeda, Manabu Kano, Shinji Hasebe, and Iori Hashimoto. Product quality estimation and operating condition monitoring for industrial ethylene fractionator. *Journal of chemical engineering of Japan*, 37(3):422–428, 2004.

23. Heon Young Yang, Sung Han Lee, and Man Gyun Na. Monitoring and uncertainty analysis of feedwater flow rate using data-based modeling methods. *IEEE transactions on Nuclear Science*, 56(4):2426–2433, 2009.

24. Shima Khatibisepehr, Biao Huang, Swanand Khare, Elom Domlan, Fangwei Xu, Aris Espejo, and Ramesh Kadali. A probabilistic framework for real-time performance assessment of inferential sensors. *Control Engineering Practice*, 26:136–150, 2014.

25. Jan Sundholm, J Gullichsen, and H Paulerpo. Mechanical pulping papermaking science and technology. *Helsinki Fapet Oy: Helsinki*, 1999.

26. Huaijing Du. *Multivariable predictive control of a TMP plant.* PhD thesis, University of British Columbia, 1998.

27. Jiyang Gao. *Modelling latency removal in mechanical pulping processes.* PhD thesis, University of British Columbia, 2014.

28. David Di Ruscio. *Topics in model based control with application to the thermo mechanical pulping process.* PhD thesis, Citeseer, 1993.

29. Mirja Illikainen. Mechanisms of thermomechanical pulp refining. *Acta Universitatis Ouluensis. Series C, Technica*, 38, 2008.

30. Hui Tian. *Stochastic multi-objective economic model predictive control of two-stage high consistency mechanical pulping processes.* PhD thesis, University of British Columbia, 2020.

31. Venkatakrishnan Venkatesh. *A systems engineering approach to effluent control, pulp characterization and process design in mechanical pulp mills.* PhD thesis, University of Idaho., 1976.

32. Gordon Broderick, Jean Paris, and Jacques L Valade. Fibre development in chemimechanical pulp refining. *Paperi ja Puu*, 79(4):193, 1996.

33. KA Kosanovich and MJ Piovoso. Process data analysis using multivariate statistical methods. In *1991 American Control Conference*, pages 721–724. IEEE, 1991.

34. Hervé Abdi. Partial least square regression (PLS regression). *Encyclopedia for research methods for the social sciences*, 6(4):792–795, 2003.

35. Behnam Talebjedi, Ali Khosravi, Timo Laukkanen, Henrik Holmberg, Esa Vakkilainen, and Sanna Syri. Energy modeling of a refiner in thermo-mechanical pulping process using ANFIS method. *Energies*, 13(19):5113, 2020.

36. Kenneth W Kolence. The software empiricist. *ACM SIGMETRICS Performance Evaluation Review*, 2(2):31–36, 1973.

37. Ray C Wang, Thomas F Edgar, Michael Baldea, Mark Nixon, Willy Wojsznis, and Ricardo Dunia. Process fault detection using time-explicit Kiviat diagrams. *AIChE Journal*, 61(12):4277–4293, 2015.

38. Jonas Mockus. Application of Bayesian approach to numerical methods of global and stochastic optimization. *Journal of Global Optimization*, 4(4):347–365, 1994.

39. Eric Brochu, Vlad M Cora, and Nando De Freitas. A tutorial on Bayesian optimization of expensive cost functions, with application to active user modeling and hierarchical reinforcement learning. *arXiv preprint arXiv:1012.2599*, 2010.

40. Carl Edward Rasmussen. Gaussian processes in machine learning. In *Summer school on machine learning*, pages 63–71. Springer, 2003.